AFRL-AFOSR-VA-TR-2021-0050

Optical Cavity Enhanced Electron Emitters

Kapadia, Rehan
UNIVERSITY OF SOUTHERN CALIFORNIA
3720 S FLOWER ST FL 3
LOS ANGELES, CA, 90007
USA

06/17/2021
Final Technical Report

Air Force Research Laboratory
Air Force Office of Scientific Research
Arlington, Virginia 22203
Air Force Materiel Command

REPORT DOCUMENTATION PAGE

Form Approved
OMB No. 0704-0188

1. REPORT DATE *(DD-MM-YYYY)*	**2. REPORT TYPE**	**3. DATES COVERED** *(From - To)*
17-06-2021	Final	15 Jul 2016 - 14 Jan 2021

4. TITLE AND SUBTITLE
Optical Cavity Enhanced Electron Emitters

5a. CONTRACT NUMBER

5b. GRANT NUMBER
FA9550-16-1-0306

5c. PROGRAM ELEMENT NUMBER

6. AUTHOR(S)
Rehan Kapadia

5d. PROJECT NUMBER

5e. TASK NUMBER

5f. WORK UNIT NUMBER

7. PERFORMING ORGANIZATION NAME(S) AND ADDRESS(ES)
UNIVERSITY OF SOUTHERN CALIFORNIA
3720 S FLOWER ST FL 3
LOS ANGELES, CA 90007
USA

8. PERFORMING ORGANIZATION REPORT NUMBER

9. SPONSORING/MONITORING AGENCY NAME(S) AND ADDRESS(ES)
AF Office of Scientific Research
875 N. Randolph St. Room 3112
Arlington, VA 22203

10. SPONSOR/MONITOR'S ACRONYM(S)
AFRL/AFOSR RTB1

11. SPONSOR/MONITOR'S REPORT NUMBER(S)
AFRL-AFOSR-VA-TR-2021-0050

12. DISTRIBUTION/AVAILABILITY STATEMENT
A Distribution Unlimited: PB Public Release

13. SUPPLEMENTARY NOTES

14. ABSTRACT
Electron emission cathodes are used in a wide variety of applications, including but not limited to, electron microscopes1,2, electron beam lithography3, space propulsion4,, high power microwave (HPM) devices5,6, 7,, free electron lasers8, and displays9. HPM sources for millimeter-wave and terahertz radiation are of great interest for military and defense applications such as radar, electronic counter measures, and communications6, 10. Electron emission cathodes are central to HPMs, and thus improvements in cathodes, such as increases in current emission capability, reduction in power, improvements in lifetime, and reduction of size/complexity directly affect the power and frequency response for a range of military and civilian applications. Traditionally, thermionic cathodes are utilized in HPMs. However, these typically require very high applied voltages, up to 500 kV to generate electron pulses and require proper thermal management to handle the high temperatures at the emitter.

15. SUBJECT TERMS

16. SECURITY CLASSIFICATION OF:			**17. LIMITATION OF ABSTRACT**	**18. NUMBER OF PAGES**	**19a. NAME OF RESPONSIBLE PERSON**
a. REPORT	**b. ABSTRACT**	**c. THIS PAGE**			JULIE MOSES
U	U	U	UU	17	**19b. TELEPHONE NUMBER** *(Include area code)* 426-9586

Optical Cavity Enhanced Electron Emitters

FA9550-16-1-0306

Final Report

7/2016-1/2021

Table of Contents

1. Report Abstract: Our focus over the course of this grant was to understand how integrated photonics and non-equilibrium electrons could be used to drive electron emission. As part of this work, we had six major achievements.

1) Demonstrated a new mechanism of hot-electron emission using integrated photonic waveguides driving graphene photoemitters and validated through detailed simulations. This mechanism enables low-optical power and low-energy photons to be used as drivers for electron emission.

2) Established the theoretical limits of hot-electron based graphene photoemitters. Through detailed simulations, we show that these devices can emit high current densities (>A/cm^2) with intrinsic response times of ~500 fs or less.

3) Experimentally shown that metal-insulator-semiconductor and graphene-insulator-semiconductor structures can be use as hot electron sources with only a voltage applied, or with both light and voltage applied.

4) Theoretically demonstrated that integrated photonics used with semiconductor negative electron affinity cathodes will break the standard trade-offs between response time, mean transverse energy, and quantum efficiency.

5) We have also shown that the hot-electron simulations developed for our devices can be used to explain experimental results obtained on non-equilibrium electrochemical reduction on gold and graphene in our group.

6) Experimentally found that a mixed electrode with graphene and LaB6 can give even higher hot-electron emission currents when compared to graphene alone. This lays the groundwork for multi-component hot electron devices.

These achievements have laid the groundwork for a new class of electron emitters which can be simultaneously bright, compact, and fast.

Products: We have produced 9 journal papers, 10 conference presentations, 3 conference papers, 1 granted patent, and three national awards partly due to the funding of this grant.

2. Introduction

Electron emission cathodes are used in a wide variety of applications, including but not limited to, electron microscopes[1,2], electron beam lithography[3], space propulsion[4,], high power microwave (HPM) devices[5,6, 7,], free electron lasers[8], and displays[9]. HPM sources for millimeter-wave and terahertz radiation are of great interest for military and defense applications such as radar, electronic counter measures, and communications[6, 10]. Electron emission cathodes are central to HPMs, and thus improvements in cathodes, such as increases in current emission capability, reduction in power, improvements in lifetime, and reduction of size/complexity directly affect the power and frequency response for a range of military and civilian applications. Traditionally, thermionic cathodes are utilized in HPMs. However, these typically require very high applied voltages, up to 500 kV to generate electron pulses and require proper thermal management to handle the high temperatures at the emitter. Furthermore, thermionic emitters, in general, are not locally addressable, and do not enable control over spatial variation of electron beams. Thus, the development of highly compact, low-power, high-speed, spatially addressable electron emission arrays would be transformative for both civilian and military applications. Towards this goal, there have been significant efforts in the development of cold-cathode field electron emission arrays, as they enable highly

compact devices, lower voltage operation through field enhancement at sharp tips, lower emittance versus thermionic sources, and simpler, room-temperature operation. However, due to the non-linear behavior of field emission versus applied field, cold-cathodes are extremely sensitive to variations in fabrication, causing non-uniform emission, limited current densities, and reliability challenges. Through the work here, we will enable high-speed arrays of electron emission cathodes which are individually addressable via photon-excitation, allowing external control of emission current from individual emitters in the array.

Two factors influence the electron emission vs voltage curves for cold cathodes at a given temperature – the work function of the emitting material and the field-enhancement factor. As the work function is not significantly tunable, once a material system has been chosen, the focus often falls on achieving the highest field-enhancement possible through geometric control of tips via micro and nanofabrication procedures. Here, we focused on a potential work-around based on photon-assisted field emission using integrated photonic components instead of cavities.

3. Hot Electron Emitters

We have shown that a waveguide integrated graphene electron emitter excited with 3.06 eV photons from a continuous wave (CW) laser exhibits two hot-electron processes that drive photoemission at peak powers >5 orders of magnitude lower than previously reported multi-photon and strong-field metallic photoemitters. Through modeling, it is shown that this reduction can be explained by two processes: (i) hot electron heating, and (ii) direct emission of excited electrons. These processes are dramatically enhanced in graphene due to the relatively weak electron-phonon coupling and the single layer structure. We also showed that the integrated photonics approach demonstrates an efficiency ~ 5100 times greater than free space excitation. The results suggest the approach of integrated photonics combined with materials exhibiting low electron-phonon coupling and thin structures, such as 2-D materials or quantum dots, could provide a rich new area for electron emitters and integrated photonic devices.

In most devices currently used, photoemission proceeds through single photon, multi-photon, or strong-field processes, with single photon being by far the most efficient of the three processes. This requires the exciting photon source to either high-energy photons, enabling single photon emission, or high-power density, enabling multi-photon or strong field emission. The present method to circumvent this challenge are negative electron affinity cathodes and other low work function materials, which allow reduction of the photon energy. Unfortunately, most low work function materials and coatings are highly unstable, causing them to be impractical for most applications. In Figure 1, we compare the behavior of our recent waveguide coupled devices to other published laser induced field emission devices[11-13] which are driven by multi-photon or strong-field emission. As most multi-photon and strong-field devices uses high peak-power pulsed lasers, we have normalized the comparison by plotting the efficiency in terms of electrons/photon vs peak power exposed to the sample. The key point behind the comparison in Figure 1 is that *waveguide integrated graphene photoemitters*

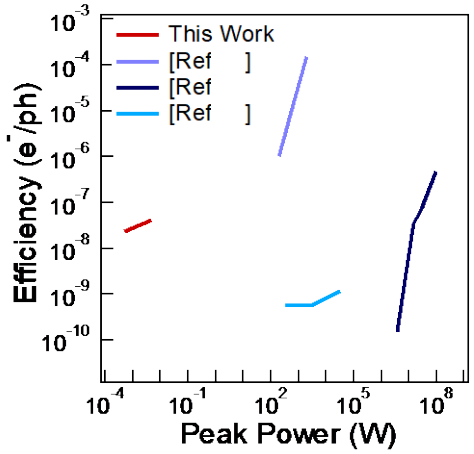

Figure 1 | Emission processes. Comparison of quantum efficiency in electrons/photon for strong-field and multiphoton emitters in literature and our integrated photonics approach (PI's work, Under Review)

exhibit electron emission at optical powers ~5 orders of magnitude lower than published reports with metal tips.

3.2 Device Structures Enabling Low-Power Emission

Figure 2a schematically illustrates the structure of the waveguide-integrated graphene electron emitter. A layer of graphene is transferred to a Si/SiO_2 substrate with a silicon nitride waveguide and gold contacts. Photons are coupled onto the chip via an optical fiber fixed to a U-groove etched into silicon and aligned to the waveguide. The free space coupled version of the emitter is shown in Figure 2b. The samples are measured in vacuum using a high-voltage source to apply the extracting field, optical fiber for laser excitation, and an ammeter for current measurement (Fig. 2c). For these measurements, the gold contacts are grounded, and the anode is held at high voltage (0-30kV). The optical absorption of graphene in the ultraviolet-visible (UV-VIS) spectrum range is primarily from interband transitions[14, 15] (Fig. 1d), with electrons excited from ½ E_{ph} below the Dirac point to ½ E_{Ph} above the Dirac point. While electrons can be excited by both single and multi-photon absorption processes, only single photon absorption is considered here due to the low optical excitation powers of <5 mW CW. In this work, 405 nm (3.06 eV) photons are

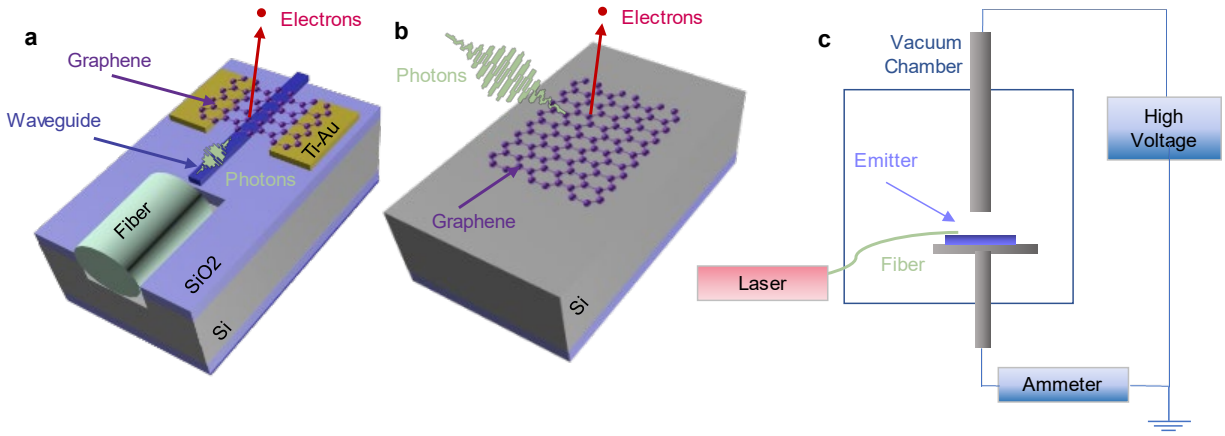

Figure 2 | Device schematics. Schematic of **a,** waveguide coupled graphene photoemitter **b,** free space coupled graphene photoemitter, and **c,** measurement setup. (PI's work, under review)

used to excite the graphene. These do not have enough energy to excite electrons above the graphene workfunction. Thus, if the optical power is below the multiphoton emission threshold, there should be no observed photocurrent unless the graphene is heated to the point that thermionic emission is significant.

Field emission characteristics for the samples schematically represented in Figure 2a and 2b were measured with and without illumination from a 405 nm laser source with the samples at room temperature and under a pressure of 5×10^{-8} Torr. Current measurements were carried out using a Keysight B2985A electrometer connected in series with our cathode to ground, and a high voltage anode was used to apply the electric fields necessary to extract electrons from the graphene. As a control sample, we characterized the electron emission from a free space laser coupled graphene sheet transferred on an n-type silicon substrate with a doping level of ~10^{19} cm^{-3}. To drive this sample optically, we illuminated the sample at an angle using the same 200 µm multimode fiber and 405 nm laser source. Figure 3a shows the results for applied electric fields up to 3 V/µm. The power incident on the sample was measured to be 190 mW. Figure 3a shows the I-E curves for graphene under free space illumination. We observed a clear, but small change in the current with illumination. After an initial rise, the overall current level does not change

significantly with applied electric field. Next, we measured the I-E curves for waveguide integrated graphene. As shown in Figure 3b, there is an initial 'turn-on' below ~0.5 V/µm, and then a steady increase of the current under illumination. The current increases by ~50x from E = 0.5 V/µm to E = 3.5 V/µm, in contrast to the free space illumination case. To understand the effect of illumination for these two devices, we plot the photocurrent, defined as $I_{PC} = I_{Light} - I_{Dark}$, in Figure 3c. For the free space case, the photocurrent is I_{PC} = 1.05 pA while the photocurrent for the waveguide integrated case is 129.3 pA for waveguide illumination. Critically, while the free space sample has ~190 mW of optical power incident upon it, the waveguide device only has ~4.6 mW of power coupled into the waveguide due to the mismatch between the fiber core size and waveguide dimensions. Using the power incident on the graphene, we plot the responsivity for the free space and waveguide coupled graphene devices (Fig. 3d). Critically, the waveguide coupled sample demonstrates a responsivity ~5100x greater than the free space sample *from an unoptimized waveguide integrated device*.

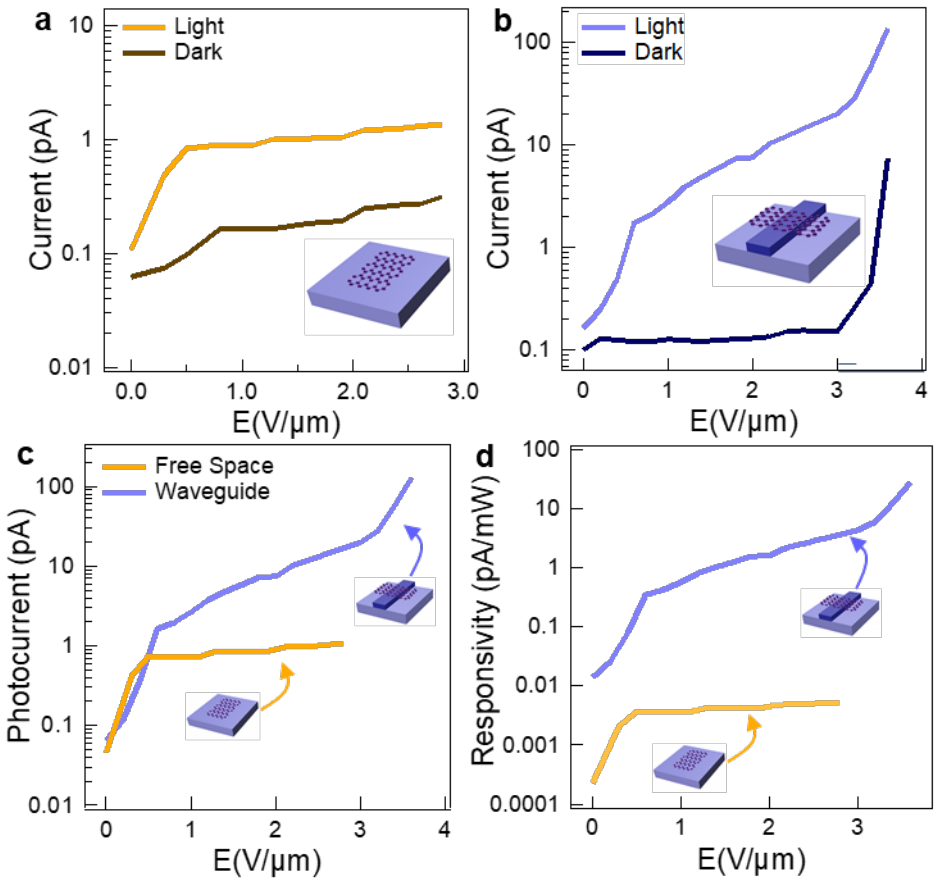

Figure 3 | Electron emission characterization. **a,** Current-Field characteristics of dark and light emission of planar graphene with free space laser coupling. **b,** Current-Field characteristics for waveguide coupled graphene. **c,** Photocurrent, defined as ($I_{Light} - I_{Dark}$) for both free-space and waveguide coupled emitters. I-time from integrated waveguide assisted graphene emitter for different laser power. **d,** Responsivity of free space and waveguide coupled cases. (PI's work, under review)

4. Multi-Component Hot Electron Emitters

However, in the previous section the large workfunction of graphene (~4.5 eV) still remains as the bottleneck to achieving even higher efficiencies from such a structure. A stable low workfunction material like LaB_6 in contact with the emitter can create a large surface dipole and reduce the overall workfunction of the emitter without sacrificing the stability of the system. Here, we have demonstrated photoemission from hybrid photoemitters composed with graphene with LaB_6 nanoparticles coupled to a CW laser (405 nm) through a waveguide. The waveguide decouples the optical absorption process from the workfunction reduction process so that graphene acts as the active absorption medium with a reduced workfunction. This hybrid photoemitter enables an efficient absorption of photons in the monolayer graphene while the LaB_6 nanoparticles reduce the workfunction of the emitter system leading to a highly efficient electron emission.

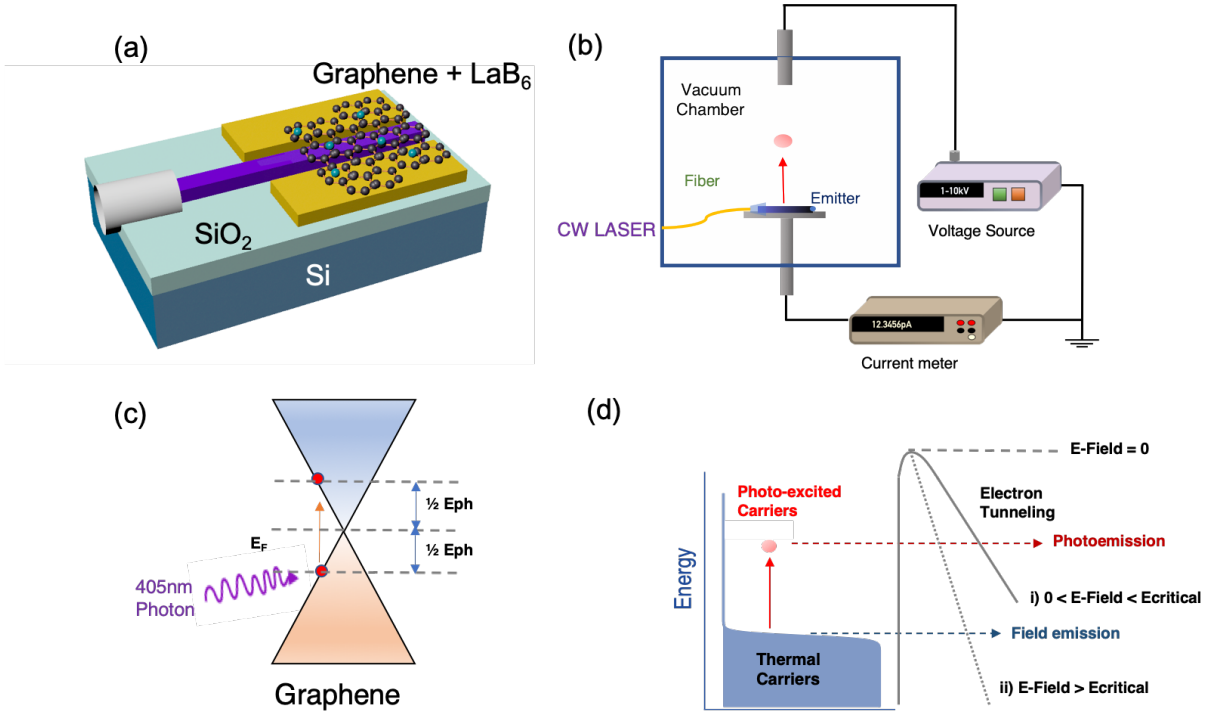

Figure 4 | Electron emission from a waveguide integrated hot electron emitter. (a) Schematic of the device and (b) the emission current measurement setup. (c) The mechanism of optical absorption in graphene (d) The mechanism of hot electron emission under an applied electric field.

Figure 4a shows the schematic of our waveguide integrated graphene electron emitter. Monolayer graphene is transferred on top of a Si_3N_4 waveguide grown by PECVD on a SiO_2/Si substrate. A gold thin film acts as the ohmic contact to the transferred graphene. Raman spectroscopy shows that graphene is indeed monolayer[16]. LaB_6 nanoparticles (~4 nm diameter) were dropcasted on top of graphene to provide

the low workfunction coating. Photons are coupled onto the chip through an optical fiber attached to a U-groove etched into silicon and aligned to the waveguide. The fiber used to couple light into the waveguide is a multimode fiber with a diameter of 200 µm, which couples not only the fundamental mode but also higher order modes into the waveguide. Figure 4b shows the system configuration for photoemission measurement. Photoemission measurement was done in vacuum condition (5×10^{-8} Torr). A DC high voltage source was used to control the anode voltage to generate the electric field required to extract the emitted electrons. A high resistance electrometer was used to measure photoemission current of device. A 405 nm CW laser (3.06 eV photon energy) is used as the optical excitation source in all the work shown in this paper. Figure 4c shows the mechanism of photon absorption in the graphene. The photons are coupled into waveguide, medium on top of the waveguide evanescently couples with the photons and eventually absorbs ~100% of them as they propagate a finite distance along the waveguide, generating

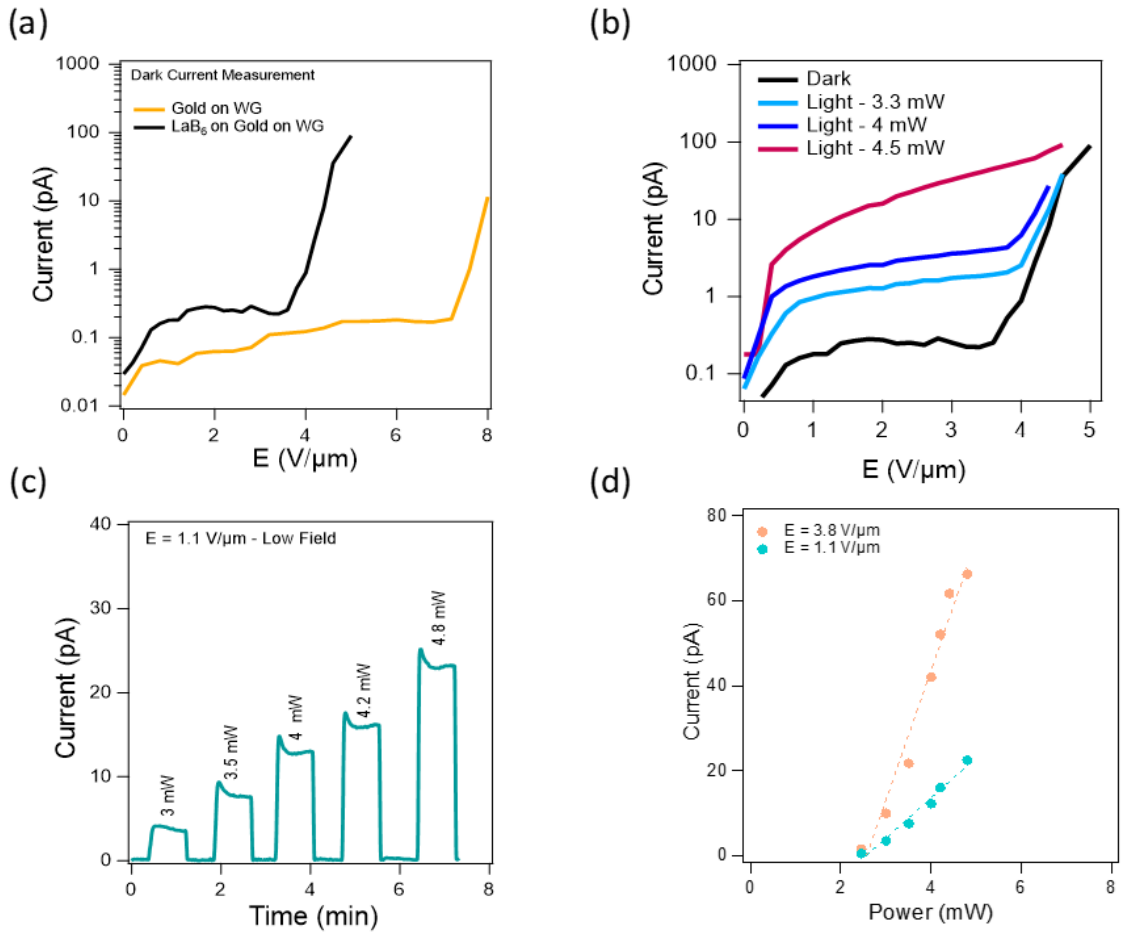

Figure 5 | LaB_6 emission characteristics on thin gold. (a) Emission I-E characteristics of thin gold with and without LaB6 in dark conditions (b) Emission current of thin gold with LaB6 emitter on waveguide at different optical powers (c) Steady state emission photocurrent measurement at a small electric field (1.1 V/µm) at different optical powers (d) Linearly change in emission current with optical power.

photoexcited electrons. The optical absorption of graphene in the ultraviolet–visible spectrum range is mainly from interband transitions, with electrons excited from ½ E_{Ph} below the Dirac point to ½ E_{Ph} above the Dirac point where E_{ph} (3.06eV) is the photon energy. Only single photon absorption is considered here due to the low optical excitation powers continuous-wave (CW) laser (< 5mW). Even though the multi n-photon absorption is a possible mechanism even at this low optical power[17-20], our previous theoretical study on multiphoton absorption in graphene rules out the possibility as that the rate of multiphoton absorption in graphene is very small compared to that of single photon absorption at the optical power densities relevant to this work[21]. Figure 4d schematically represents the mechanism of emission of electrons from graphene. There are two different types of electrons in graphene that lead to two distinct emission procedures: (i) emission of photoexcited electrons before thermalization which is dominant below a critical field ($E_{Critical}$), and (ii) field emission of the cold electrons, which is independent of photon absorption and dominant above $E_{Critical}$. In the presence of a vertical electric field, the photoexcited electrons can tunnel through the bent vacuum barrier to contribute to the emission current. Since the photoexcited electrons experience a smaller tunnel barrier as compared with the thermal carriers, photoexcited nonequilibrium electrons will dominate the emission currents below a certain critical electric field while the large population of thermal electrons will dominate emission above the critical electric field.

Lowering the workfunction or electron affinity of an emitter usually requires a strong electric dipole on top of the emitter such as cesium fluoride or cesium oxide coating. However, such coatings are extremely unstable under ambient conditions and require vacuum levels lower than 10^{-9} Torr. LaB_6 has a small workfunction[22] (2.7eV) and it is air stable compared to the low workfunction alkali metals. A coating of LaB_6 on top of a metallic emitter can also create a strong electric dipole due to the workfunction difference of the emitter and LaB_6. In this work, we have compared two different emitters with LaB_6 nanoparticle coating: graphene and 10nm of thin gold layer. Both graphene and thin gold can absorb the photons traveling through the waveguide. Using a thin gold film or monolayer graphene ensures that the photoexcited electrons are always close to the emitting surface and therefore reduces the transit time to the surface. When the photoexcited electrons transit to the emitter surface, they go through different scattering mechanisms and lose energy drastically. Therefore, this reduction in transit time is of great benefit to increase photoemission efficiency.

First, we investigated a hybrid thin gold film emitter coated with the LaB_6 nanoparticles integrated to the optical waveguide. Figure 5a compares the dark emission current performance of two gold emitters with and without the LaB_6 nanoparticles. It can be observed that the dark current threshold field of the bare gold is larger (7 V/μm) compared to the dark current threshold field of the LaB_6 nanoparticles on gold (3.5 V/μm). By using this hybrid structure, the dark and light I-E emission characteristics of LaB_6 nanoparticles on gold is shown in Figure 5b. These results show that the photon assisted emission current is detected at E- field as small as 0.5 V/μm. As expected, higher intensity photon gives higher photoemission currents. For the 4.5 mW case, the photoemission current reaches up to 10pA even under E-field < 2 V/μm. Above a critical field of ~ 3.8 V/μm, the field emission current due to the thermal electrons of gold becomes more dominant compared to the photoemission current. The current vs time measurement for LaB_6 on gold emitter on waveguide at different laser powers is shown in Figure 5c. Low E-field (1.1 V/μm) was used here to eliminate the possibility of emission coming from thermal cold electrons. The increase in emission current with increasing laser power and the sharp change in current due to switching the laser verifies the photoemission in our hybrid photoemitter. The spikes are coming out at the initial turn on of the laser due to the fast modulation of laser light. The separate test on the effect of laser modulation on emission current shows 15-20 sec is needed for transient signals to reach to steady state as shown in Supplementary Figure 3. Figure 5d shows the linear relationship between optical

power densities and emission current which suggests that only the first order single photon absorption process is dominant in the system.

5. Theoretical Limits of Graphene Emitters

The unique linear band structure of graphene allows its electrons to be excited directly from the valence band to the conduction band within photon energies ranging from far IR to UV. These photoexcited electrons, referred to as "hot electrons," in graphene are out of equilibrium compared to the initial electron distribution. These nonequilibrium hot electrons therefore go through different scattering mechanisms where they lose energy and thermalize. The most prominent scattering mechanisms in graphene are: (1) electron-electron (e-e) scattering, (2) optical phonon (OP) scattering, and (3) supercollision acoustic phonon (SC) scattering[23-28]. While e-e scattering allows the hot electrons to elastically redistribute their excess energy among the "cold" electrons in the Fermi sea, both OP and SC scattering cause them to lose energy to the lattice. When a vertical electric field is applied to graphene, the vacuum barrier bends in response to the field and these hot electrons can tunnel through the distorted

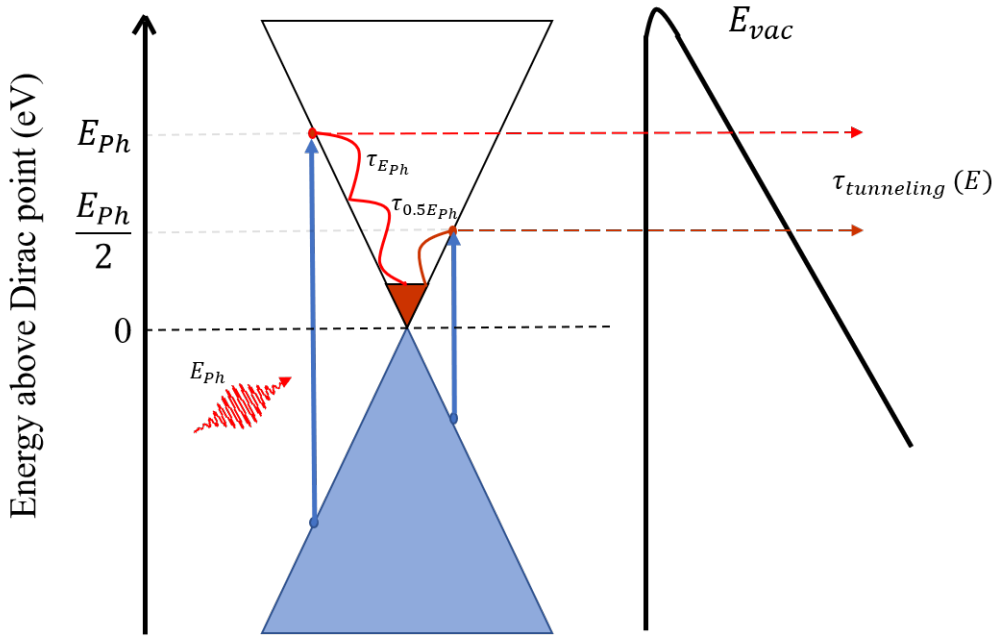

Figure 6 | Emission of photogenerated hot electrons from graphene while they go through the scattering processes

vacuum barrier. In addition to the usual scattering mechanisms, this tunneling mechanism provides another possible pathway for the hot electrons to reach a different final state[23, 24]. Probability rates of these mechanisms depend on the energy and momenta of the involved electrons, phonons as well as the bandstructure of graphene and can be quantitatively calculated using Fermi's golden rule. Figure 6 summarizes the basic mechanism of electron emission from graphene.

To quantitatively evaluate the electron emission current from graphene as a function of photon energy, optical power density and electric field, it is important that we quantitatively determine the rates of the scattering mechanisms and tunneling. Here, Fermi's golden rule is used to calculate the rates[23, 29]:

$$\frac{1}{\tau} = \frac{2\pi}{\hbar}\sum_{k,k'}|M(k,k')|^2(1-f(k'))\delta_E \qquad (1)$$

Here, $\frac{1}{\tau}$ is the scattering rate, $M(k,k')$ is the matrix element for the transition between the initial state $|k\rangle$ to the final state $|k'\rangle$, f(k) is the Fermi-Dirac distribution, and δ_E ensures the energy conservation. For different scattering mechanisms, the matrix element will be different and therefore will lead to different scattering rates. Calculation of each of the scattering rates have been carried out[23].

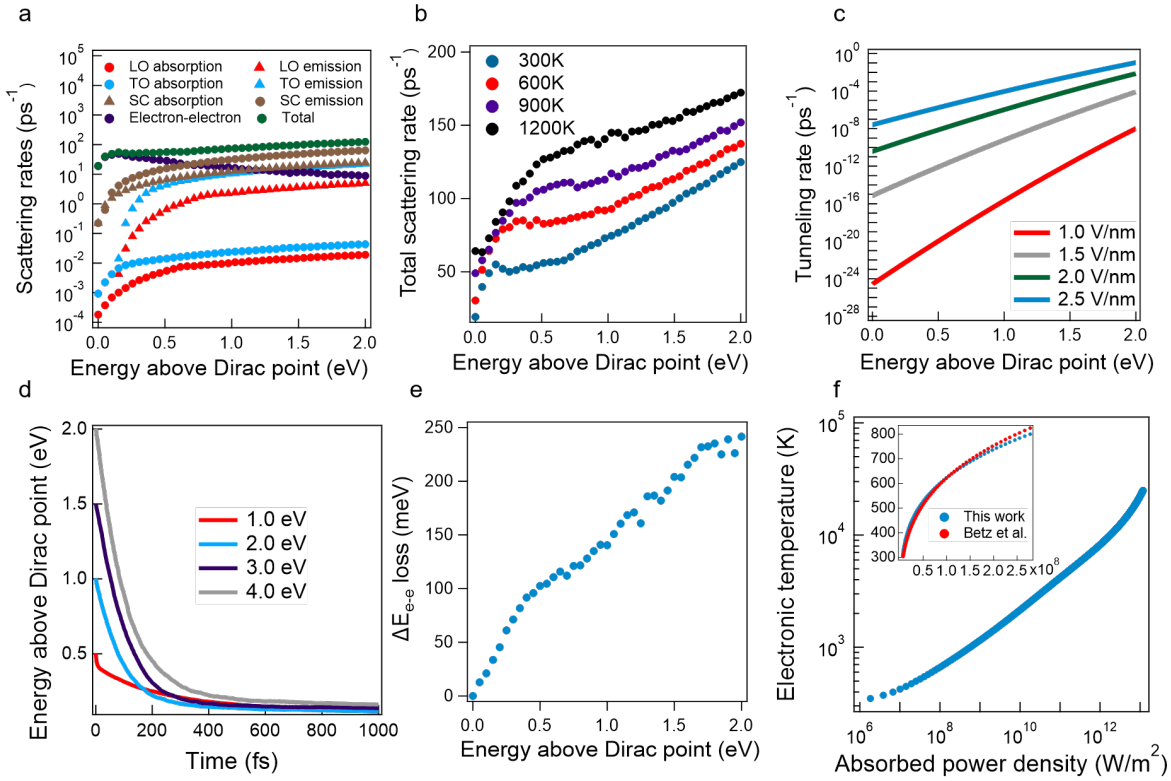

Figure 7 | Simulation of hot electron scattering, electron emission and electronic temperature. a, hot electron scattering rates for the major scattering mechanisms of graphene for electronic temperature of 300K. b, total scattering rates for different electronic temperatures. c, energy resolved tunneling rates for hot electrons in graphene. d, simulated time resolved energy trajectory of hot electrons excited by different photon energies. e, average energy lost by hot electrons due to e-e scattering. f, simulated electronic temperature of graphene as a function of absorbed optical power density.

Figure 7a shows the scattering rates for all the scattering mechanisms as a function of electron energy for an electronic temperature of 300K while figure 7b summarizes the total scattering rates for different electronic temperatures. Since increasing electronic temperature increases the number of electrons in the Fermi sea, the e-e scattering increases significantly. This ultimately leads to an increase in the overall

scattering rates with increasing electronic temperature. The tunneling rates for different electric fields are shown in figure 7c. Electrons with higher energy see a smaller barrier and therefore have larger tunneling rates. On the other hand, when electric field is increased, the nearly triangular vacuum barrier is further thinned and there is an exponential increase in the tunneling rate. Therefore, an electron with higher energy will be able to tunnel the barrier more frequently if a larger electric field is applied.

The MCBTE simulation uses the calculated scattering rates to determine the energy-time trajectory of the hot electrons. The simulation is initialized with 5 million electrons which is equivalent of simulating 0.5 μm^2 of graphene. Figure 7d shows the calculated trajectories for four different photon energies when the electronic temperature is 300K. The trajectories have been obtained by tracking the average energy of 50 photoexcited electrons during each simulation and then averaging over 50 different simulations. The trajectory for 1 eV photons shows us three distinct regions: (1) an initial drop in electron energy due to e-e scattering, (2) dissipation of energy due to OP scattering until the electron energy goes below the OP energy (~190 meV), and (3) a slower dissipation in energy due to SC scattering. Since e-e scattering rates are considerably smaller than the OP scattering rates for higher energy electrons, the e-e scattering dominated initial energy loss cannot be observed in the trajectories obtained for higher energy photons. Average energy loss of hot electrons due to e-e scattering events has been shown in figure 7e. Figure 7f shows the change in electronic temperature as a function of absorbed optical power density. Using these scattering rates, the calculated electronic temperature profile is shown to match the temperature experimentally observed by Betz et al[23, 26].

A. Emission current model:

We have modeled the emission current using a quantum mechanical tunneling model[23]. The current density due to the thermalized electrons of graphene, also known as thermionic-field emission (TFE) current density, can be expressed as

$$J_{TFE}(T,F) = e\int_{-\infty}^{\infty} D(E)Tr(E,F)f(E,T)dE \qquad (2)$$

Here, T is the electronic temperature, E is the energy of the electron, F is the electric field, e is the elementary charge, $D(E)$ is the density of states of graphene, $Tr(E,F)$ is the tunneling rate and $f(E,T)$ is the Fermi-Dirac distribution. For different optical power densities, we find the electronic temperature from figure 7f and evaluate the integral numerically to calculate the current density due to the thermal electrons.

In order to calculate the emission current due to photoexcited electrons, we consider the possibility of multiphoton absorption (MPA)[30, 31] so that every absorbed photon results in *n* photoexcited electron-hole pairs for *n* photon absorption and therefore calculate the generation rate from the relation, $S = \sum_{i=1}^{n} G_i(S, E_{Ph})E_{Ph} \times i$. Here, S is the absorbed power density and $G_i = \frac{\tau_1}{\tau_i}G_1$ is the generation rate for the *i*-photon absorption process. We have explained the details of the calculation of the *i*-photon absorption rate, τ_i in the supplementary information. Figure 8a shows the ratio of two photon absorption (TPA) rate to single photon absorption (SPA) rate for different photon energies and power densities. Now, we can calculate the emission current due to hot electrons (HE) from the following relation[23]

$$J_{HE}(S,F) = \sum_{i=1}^{n}\int_{0}^{\infty} eG_i(S,E_{Ph})Tr(E(t),F)dt \qquad (3)$$

Here, $E(t)$ is the energy of the hot electron as a function of time as shown in figure 2d where $E(0) = \frac{nE_{Ph}}{2}$ for n photon absorption.

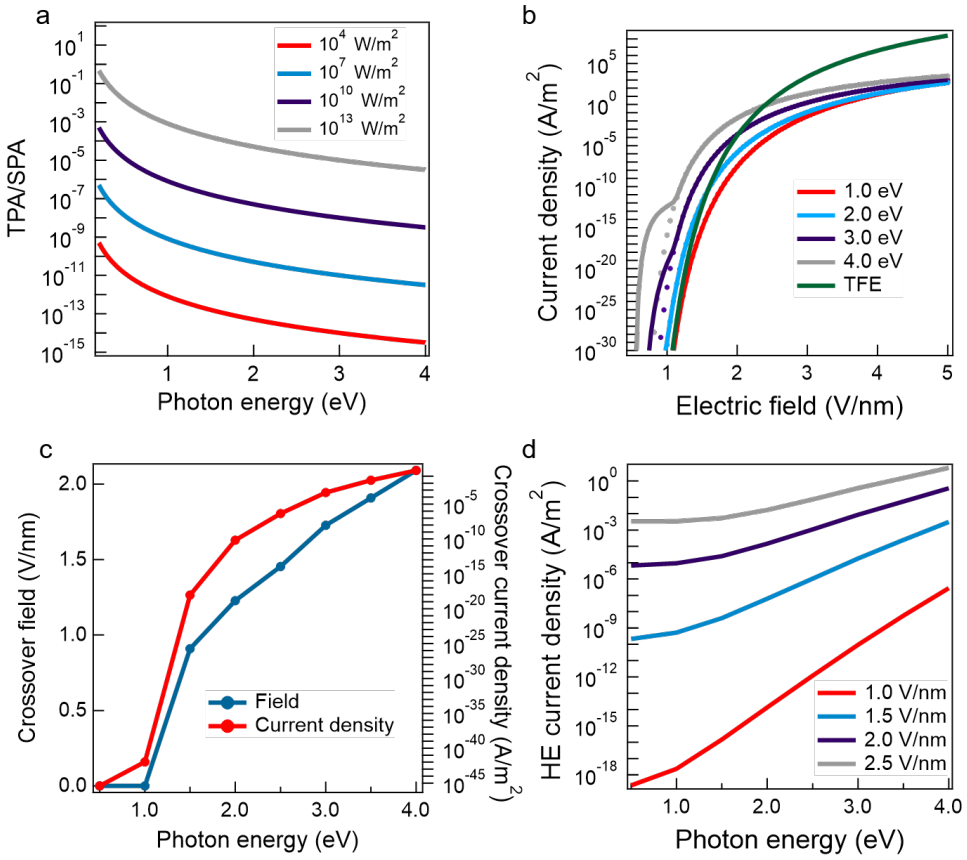

Figure 8 | Electron emission current calculation for low power density photoexcitation. a, ratio of TPA rate to SPA rate in graphene different absorbed power densities. b, simulated HE and TFE current density for different photon energies at an absorbed power density of 10^4 W/m^2 (dots: SPA, connected lines: MPA). c, crossover electric field and current densities as a function of photon energy. d, HE current density as a function of photon energy for different electric fields

Using these relationships, we have calculated the current densities for four different photon energies (1-4 eV) for a power density of 10^4 W/m^2 as we varied the electric field from 0.5 to 5 V/nm. The reason behind choosing 10^4 W/m^2 is to investigate the current density when there is no significant heating of the electron population. We ignore electronic temperature deviation below a power density of ~10^6 W/m^2, as the electronic temperature does not deviate significantly. We have considered MPA processes to order, $n = 3$ for $E_{Ph} = 1, 2$ eV and $n = 2$ for $E_{Ph} = 3, 4$ eV. Figure 8b shows the calculated hot electron current densities for different photon energies as well as the TFE current density. At smaller electric fields, the thermal electrons see a wider and larger energy barrier for tunneling whereas the high energy electrons see a narrower and smaller energy barrier. Therefore, the hot electron component dominates at

the smaller electric fields over the thermal component as observed for the case of higher energy photons (>1 eV). At even smaller electric fields, the MPA processes dominate over SPA for higher photon energies. There are two competing factors that determine whether SPA or MPA process will dominate the observed current density: (1) energy of the hot electron and (2) efficiency of the MPA process. The initial energy difference between an electron that absorbed one photon and an electron that absorbed *n* photons is the energy of *(n-1)* photons. The tunneling rate increases exponentially with the increase in electron energy[23]. However, the magnitude of current density due to MPA at these conditions is below the threshold current density likely to be observed in an experiment. From figure 8b, we can observe a clear crossover between the hot electron dominated regime and the TFE dominated regime. However, for 1 eV photons and below, the hot electron current is not significant enough within the electric field range considered and no crossover can be observed. Figure 8c shows the crossover fields and current densities as a function of photon energy. For higher photon energies, the crossover field increases at a nearly linear rate and therefore the crossover current densities increase by several orders of magnitude. Figure 8d shows the hot electron current density as a function of photon energy for different electric fields. We can see an exponential increase in current density with increasing photon energies. However, the increase is less steep for larger electric fields as the barrier gets thinner and the difference in barrier heights play a less effective role in determining the tunneling rates. For lower photon energies, the difference in barrier heights is even smaller and the increase in HE current is even less prominent. The most significant observation from these calculations is that there exists a distinct crossover field for every photon energy below which hot electrons will dominate the emission current and for the same power density of different photon energies and the same electric field below the crossover field, the efficiency of converting photons

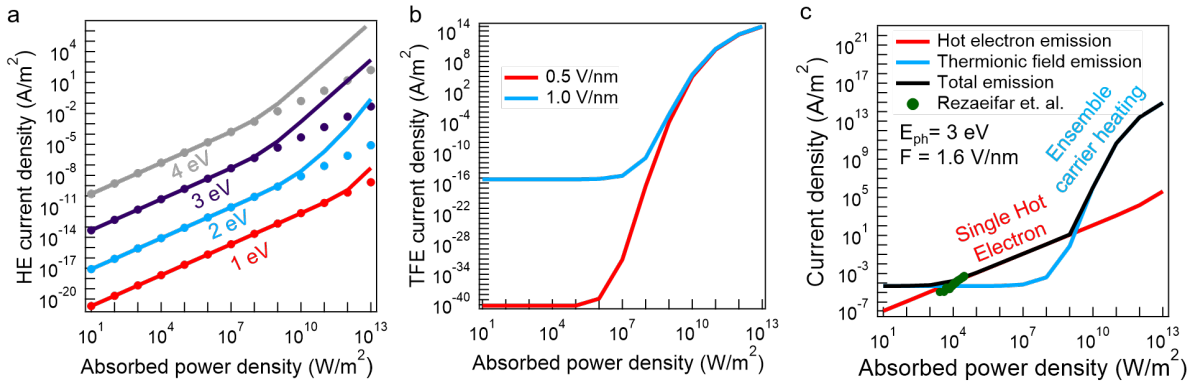

Figure 9 | Electron emission current calculation for large power densities. a, calculated HE current density for different photon energies at an electric field of 1.0 V/nm (dots: SPA, connected lines: MPA). b, calculated TFE current density at 0.5 V/nm and 1.0 V/nm fields. c, crossover between different emission mechanisms at different ranges of absorbed power densities calculated at 1.6 V/nm for photoexcitation by 3 eV photons.

to emitted electrons will be higher for higher photon energies.

For power densities >10^6 W/m^2, the electron population will heat up to a temperature that is significantly greater than the lattice temperature (300K). In addition to cold field emission and single hot electron emission, this electronic heating leads to the emission of ensemble hot electrons. Figure 9a shows the calculated HE current densities for an electric field of 1 V/nm considering the different hot electron trajectories obtained for the electronic temperatures produced by the corresponding power densities. MPA processes exceed the SPA process only at higher power densities. The corresponding TFE current

densities due to ensemble carrier heating are shown in Figure 9b. For power densities > 10^9 W/m^2, the electronic temperature rises above 1000K and the effect of increasing electric field becomes insignificant. Figure 9c shows the different components of the total emission current density for $E_{Ph} = 3$ eV and $F =$ 1.6 V/nm. Here, we can identify three different mechanisms of electron emission that dominate at different ranges of power densities: (1) field emission at small power densities, (2) single hot electron emission at intermediate power densities, and (3) ensemble hot electron emission at large power densities, Since both hot electron generation rate and electronic heating are small at smaller power densities, this regime is dominated by the tunneling of thermal electrons within few $k_BT(\sim 26\ meV)$ of the Fermi level, i.e., cold field emission. For intermediate power densities, electronic heating is still insignificant whereas the generation rates increase proportionally and hence this regime is dominated by the single hot electron emission. Beyond this regime, the electronic heating becomes more significant and thermionic emission due to ensemble hot electrons dominates. Figure 9c also shows the experimentally measured electron emission current from Fatemeh et. al. for the same electric field and photon energy which shows a good agreement to our theoretical values [23].

5. Output

The overall output of this grant has been 9 peer-reviewed journal papers, 3 conference papers, 3 national level awards, and 1 patent. It has also trained 2 postdoctoral researchers, 3 graduate students, and two undergraduates.

Awards

1. IVEC Best Student Paper Award, Fatemeh Rezaeifar, 2018
2. AVS Peter Mark Memorial Award, Rehan Kapadia 2020
3. ONR YIP Award, Rehan Kapadia 2021

Patents:

1. F. Rezaeifar, R. Kapadia, "Optical Modulation of on-chip thermionic emission using resonant cavity coupled electron emitters", US Patent 10,403,484 (2019)

Journal Papers:

1. H. U. Chae, R. Ahsan, J. Tao, S. B Cronin, and R. Kapadia. "Metal Free Hot Electron Driven Electrode Assisted by Plasma Etched Graphene for Hydrogen Evolution Reaction", *Advanced Materials Intefaces*, 8 (6) 2001706, 2021.
2. F. Rezaeifar., H. U. Chae, R. Ahsan, R. Kapadia. "Hot electron emission from waveguide integrated lanthanum hexaboride nanoparticles", *Applied Physics Letters*, 118 (7), 071108, 2021.
3. H.U. Chae, R. Ahsan, J. Tao, R. Kapadia, "Tunable Onset of Hydrogen Evolution on a Graphene-Insulator-Semiconductor Hot Electron Device", *Nano Letters,* 20 (3), 1791-1799, 2020.
4. R. Ahsan, M.S. Sakib, H.U. Chae, R. Kapadia, "Performance limits of graphene hot electron emission photoemitter", *Physical Review Applied*, 13 (2), 024060, 2020.
5. H.U. Chae, R. Ahsan, Q. Lin, D. Sarkar, S.B. Cronin, R. Kapadia, "High Quantum Efficiency Hot Electron Electrochemistry", *Nano Letters*, 19 (9), 6227-6234, 2019.
6. F. Rezaeifar, R. Ahsan, Q. Lin, H. U. Chae, R. Kapadia, "Hot-electron emission processes in waveguide-integrated graphene", *Nature Photonics*, 13, 843-848, 2019.

7. L. Blankemeier, F. Rezaeifar, A. Garg, R. Kapadia, “Integrated Photonics for Low Transverse Emittance, Ultrafast Negative Electron Affinity GaAs Photoemitters". *Journal of Applied Physics*, 126, 3, 033102, 2019.
8. F. Rezaeifar, Q. Lin, A. Garg, N. Poudel, L. Blankemeier, D. Sarkar, X. Chen, A. Clough, T. Mattox, S. Cronin, and R. Kapadia. “Independent tuning of work function and field enhancement factor in hybrid lanthanum hexaboride-graphene-silicon field emitters”, *Journal of Vacuum Science and Technology B*, 35 (6) 062202, 2017.
9. F. Rezaeifar, R. Kapadia, “Efficient and Ultrafast Optical Modulation of On-Chip Thermionic Emission Using Resonant Cavity Coupled Electron Emitters”, *Journal of Vacuum Science & Technology B*, 34 (4), 041228, 2016.

Conference Papers:

10. F. Rezaeifar, R. Kapadia,"Cavity coupled photon-enhanced thermionic electron emitter", 2016 IEEE International Vacuum Electronics Conference (IVEC), DOI: 10.1109/IVEC.2016.7561781
11. F. Rezaeifar, R. Kapadia, "Engineering the Field Enhancement Factor and Work Function toward Ultra-Low Threshold Field Electron Emitter", 2018 IEEE International Vacuum Electronics Conference (IVEC), DOI: 10.1109/IVEC.2018.8391490
12. F. Rezaeifar, R. Kapadia, "Integrated Waveguide Assisted Electron Emission Device", 2018 IEEE International Vacuum Electronics Conference (IVEC), DOI: 10.1109/IVEC.2018.8391491

6. References

1. Goldstein, J.; Newbury, D. E.; Echlin, P.; Joy, D. C.; Romig Jr, A. D.; Lyman, C. E.; Fiori, C.; Lifshin, E., *Scanning electron microscopy and X-ray microanalysis: a text for biologists, materials scientists, and geologists*. Springer Science & Business Media: 2012.
2. Reimer, L., *Transmission electron microscopy: physics of image formation and microanalysis*. Springer: 2013; Vol. 36.
3. Vieu, C.; Carcenac, F.; Pepin, A.; Chen, Y.; Mejias, M.; Lebib, A.; Manin-Ferlazzo, L.; Couraud, L.; Launois, H. *Applied Surface Science* **2000,** 164, (1), 111-117.
4. Goebel, D. M.; Katz, I., *Fundamentals of electric propulsion: ion and Hall thrusters*. John Wiley & Sons: 2008; Vol. 1.
5. Benford, J.; Swegle, J. A.; Schamiloglu, E., *High power microwaves*. CRC Press: 2007.
6. Gold, S. H.; Nusinovich, G. S. *Review of Scientific instruments* **1997,** 68, (11), 3945-3974.
7. Barker, R. J.; Luhmann, N. C.; Booske, J. H.; Nusinovich, G. S. *Modern Microwave and Millimeter-Wave Power Electronics, by Robert J. Barker (Editor), Neville C. Luhmann (Editor), John H. Booske (Editor), Gregory S. Nusinovich, pp. 872. ISBN 0-471-68372-8. Wiley-VCH, April 2005.* **2005,** 1.
8. Brau, C. A. **1990**.
9. Wang, Q.; Setlur, A.; Lauerhaas, J.; Dai, J.; Seelig, E.; Chang, R. *Applied Physics Letters* **1998,** 72, (22), 2912.
10. Kartikeyan, M. V.; Borie, E.; Thumm, M., *Gyrotrons: high-power microwave and millimeter wave technology*. Springer Science & Business Media: 2013.
11. Bormann, R.; Gulde, M.; Weismann, A.; Yalunin, S.; Ropers, C. *Physical review letters* **2010,** 105, (14), 147601.
12. Barwick, B.; Corder, C.; Strohaber, J.; Chandler-Smith, N.; Uiterwaal, C.; Batelaan, H. *New Journal of Physics* **2007,** 9, (5), 142.
13. Yang, D.-S.; Mohammed, O. F.; Zewail, A. H. *Proceedings of the National Academy of Sciences* **2010,** 107, (34), 14993-14998.
14. Falkovsky, L. In *Optical properties of graphene*, Journal of Physics: Conference Series, 2008; IOP Publishing: p 012004.
15. Falkovsky, L.; Pershoguba, S. *Physical Review B* **2007,** 76, (15), 153410.
16. Wang, Y. Y.; Ni, Z. H.; Yu, T.; Shen, Z. X.; Wang, H. M.; Wu, Y. H.; Chen, W.; Shen Wee, A. T. *The Journal of Physical Chemistry C* **2008,** 112, (29), 10637-10640.
17. Zhang, P.; Lau, Y. *Scientific reports* **2016,** 6, 19894.
18. Zhou, Y.; Zhang, P. *Journal of Applied Physics* **2020,** 127, (16), 164903.
19. Luo, Y.; Zhang, P. *Physical Review B* **2018,** 98, (16), 165442.
20. Luo, Y.; Zhang, P. *Physical Review Applied* **2019,** 12, (4), 044056.
21. Ahsan, R.; Sakib, M. A.; Chae, H. U.; Kapadia, R. *Physical Review Applied* **2020,** 13, (2), 024060.
22. Goebel, D.; Hirooka, Y.; Sketchley, T. *Review of Scientific Instruments* **1985,** 56, (9), 1717-1722.
23. Rezaeifar, F.; Ahsan, R.; Lin, Q.; Chae, H. U.; Kapadia, R. *Nature Photonics* **2019**, 1-6.
24. Ma, Q.; Andersen, T. I.; Nair, N. L.; Gabor, N. M.; Massicotte, M.; Lui, C. H.; Young, A. F.; Fang, W.; Watanabe, K.; Taniguchi, T. *Nature Physics* **2016,** 12, (5), 455.
25. Breusing, M.; Kuehn, S.; Winzer, T.; Malić, E.; Milde, F.; Severin, N.; Rabe, J.; Ropers, C.; Knorr, A.; Elsaesser, T. *Physical Review B* **2011,** 83, (15), 153410.
26. Betz, A.; Jhang, S. H.; Pallecchi, E.; Ferreira, R.; Fève, G.; Berroir, J.-M.; Plaçais, B. *Nature Physics* **2013,** 9, (2), 109.
27. Song, J. C.; Reizer, M. Y.; Levitov, L. S. *Physical review letters* **2012,** 109, (10), 106602.
28. Brida, D.; Tomadin, A.; Manzoni, C.; Kim, Y. J.; Lombardo, A.; Milana, S.; Nair, R. R.; Novoselov, K. S.; Ferrari, A. C.; Cerullo, G. *Nature communications* **2013,** 4, 1987.

29. Chae, H. U.; Ahsan, R.; Lin, Q.; Sarkar, D.; Rezaeifar, F.; Cronin, S. B.; Kapadia, R. *Nano letters* **2019,** 19, (9), 6227-6234.
30. Faisal, F. H. *Annalen der Physik* **2013,** 525, (1-2), 171-179.
31. Faisal, F. H., *Theory of multiphoton processes*. Springer Science & Business Media: 2013.